DEEP LEARNING-BASED DETECTION, SEGMENTATION AND AVERAGE AREA ESTIMATION OF CELLS

Xhoena POLISI DURO
Department of Informatics, Fan S. Noli University, Korça, Albania
Department of Computer Engineering, EPOKA University, Tirana, Albania

Vule SHARKA, Arban UKA, Dimitrios A. KARRAS
Department of Computer Engineering, EPOKA University, Tirana, Albania

Albana NDREU HALILI
Department of Medicine, Faculty of Technical Medical Sciences, Western Balkans University, Tirana, Albania
Corresponding author: xpolisi@epoka.edu.al

ABSTRACT

Evaluation of cell shape parameters in microscopy images is essential for medical image analysis because: i) supports the development of automatic blood cell analysers, ii) facilitates cell image classification, and iii) aids in cell health evaluation. Staining is a fundamental technique used in biology and medical fields that enhances visibility of miroorganisms or cells that are difficult to distinguish. This process involves adding colour or chemical dyes to specimens to increase their contrast under a microscope. However, many experimental conditions do not allow staining, making unstained brightfield microscopy the only feasible solution. This handicap is the most challenging problems in medical imaging. The present paper aims to count and evaluate cell shape parameters in unstained images and to deduce the cell health states. A unique dataset including cells that reside in environments with different toxicity levels. The health state of cells is correlated with morphological parameters such as the shape (which is inherently deformable), texture and area of the cells. The present paper reports the application of modern deep learning architectures in cell counting and cell area determination. The results show a correlation between morphological changes and environmental toxicity levels in which the cells reside.

Keyword(s): unstained Brightfield images, biomaterial toxicity, cell segmentation, U-NET architecture

1. INTRODUCTION

Research in medical sciences relies heavily on microscopy imaging as a non-invasive tool for diagnosis and treatment evaluation. Advancements in microfluidics and single-cell technologies, single- cell manipulation have made separation and isolation possible (Whitesides, 2006; Baysoy *et al*., 2023). Over the past two decades, the advancements in fabricating precise microfluidic chambers have provided not only greater control of the experimental plate but also the ability to use micropatterned surfaces to test cell attachment, cell growth etc. (Uka *et al*., 2017; Schurr *et al*., 2022). Once properly isolated in multiparametric microfluidic chambers, cells can be treated and monitored though imaging technologies at controllable throughput (Rane *et al*., 2017). Imaging technologies include the use of portable brightfield microscopy (Ozcan 2014; Göröcs *et al*., 2018), digital in-line holography (Martin *et al*., 2022), computational imaging (Uka *et al*., 2022) and computation on portable computing units (Uka *et al*., 2021; Polisi *et al*., 2023). An important area of research that relies heavily on imaging technologies to study biological systems at the cellular level is biomaterial risk assessment (Dollinger *et al*., 2017; Gribova *et al*., 2023). In these settings medical practitioners need to evaluate personalized level biotoxicity tolerance of a patient against a series of potential biomaterials for a specific transplant. The toxicity levels of a biomaterial can be assessed through a series of measurements conducted in microfluidic chambers, including impedance measurement (Chmayssem *et al*., 2021; Chmayssem *et al*., 2022), chronoamperometric measurements (Rodrigues *et al*., 2008; Dincer *et al*., 2022), genotoxicity (Li *et al*., 2018), microscopy (Polisi *et al*., 2020; Uka *et al*., 2021), pH measurement (Tovar *et al*., 2020; Magnusson *et al*., 2013) etc. When conducting work on these chambers, a fundamental requirement is minimizing or completely eliminating the interference of different data acquisition tools. To obtain accurate impedance or chronoamperometric measurements, it is essential to reduce the presence of free ions as much as possible. This constrain prevents using staining as a procedure, making unstained brightfield imaging the only available solution. However, the quality of the images is diminished, and the contrast remains low, as the images have to be acquired within microfluidic chips where cells are floating in fluids that provide nutrition to the cells. The variations on the index of refraction of the material of the chamber and of the fluids negatively affects the quality of the images. The fluids are mostly

hydrogels, which mimic the extracellular matrix present in the biological systems. These hydrogels supply nutrients and support cell growth for the cells as the cells are monitored over a two-weeks period. However, these hydrogels that limits the use other imaging modalities such as phase contrast microscopy etc. The low contrast at the edges of the cytoplasm would create difficulties in correctly providing a quantitative measure of the changes in the cell texture and morphology. Some images have few hundreds of cells, and an automated counting would be the only appropriate solution to save medical practitioners' time. To develop optimal solutions for various datasets, several challenges are introduced at leading conferences, where datasets are manually labelled to establish a consistent ground truth for image analysis.

The 2018 Data Science Bowl is a relevant challenge with a focus on cell nuclei segmentation from microscope images (Caicedo *et al.*, 2019). This served as a good platform to work on and to develop models that would segment nuclei from stained cells from fifteen biological studies across different experimental conditions. The researchers compiled a collection of 37,333 manually labelled nuclei in 841 2D images from over thirty trials involving various samples. Due to the inherent difficulty, of very low contrast the organizers of the challenge had intentionally excluded electron microscope and unstained brightfield images (Caicedo *et al.*, 2019). Figure 1 depicts the images here reported.

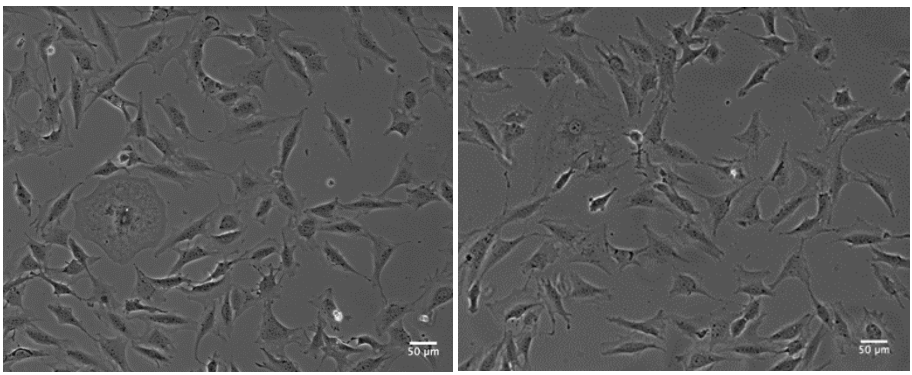

Fig. 1: Samples of the images of the cells to be analysed.

The top solutions to the challenge involved the use of deep neural networks. Key elements are: i) sophisticated data augmentation and data post-processing (best performing solution), ii) careful use of loss function (second best solution), and iii) use of Mask-RCNN architecture. An important finding here reported was that the variation between manually annotated images by different practitioners was larger than the difference between a labeller and a trained model. Figure 2 depicts these results. We observed a similar behaviour represented by a 1-2% difference between two different labellers for the same image. In automated cell image classification pre-processing in both the spatial domain. and in the frequency domain is reported to be very important in overall cell classification (Uka *et al*., 2020; Polisi *et al*., 2023).

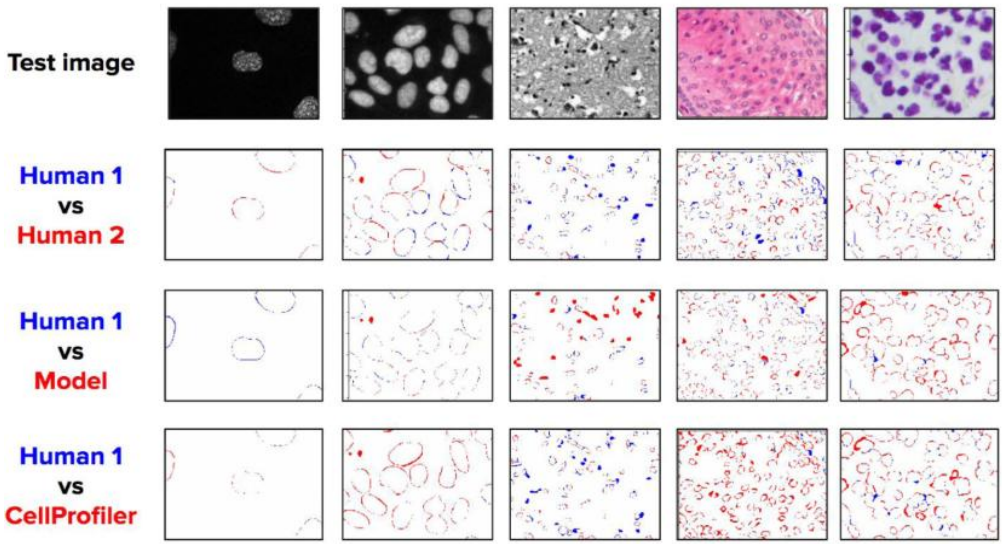

Fig. 2: Image Annotations, courtesy of (Caicedo *et al*., 2019).

Other intuitive techniques have proven to improve the overall accuracy in cell nuclei segmentation. Budginaitė *et al*., (2021) presented an end-to-end deep learning-based system for cell nuclei segmentation and consecutive lymphocyte identification in H&E-stained 20 magnified breast and colorectal cancer images. This study also showed that nuclei annotation masks with an additional active contour layer will improve nuclei segmentation accuracy by 1.5 percent.

U-Net architecture variations have proven successful on several datasets. Long presented a lightweight U-Net (called U-Net+) with a modified encoded branch capable of low-resource computations (Long *et al*.,2020).

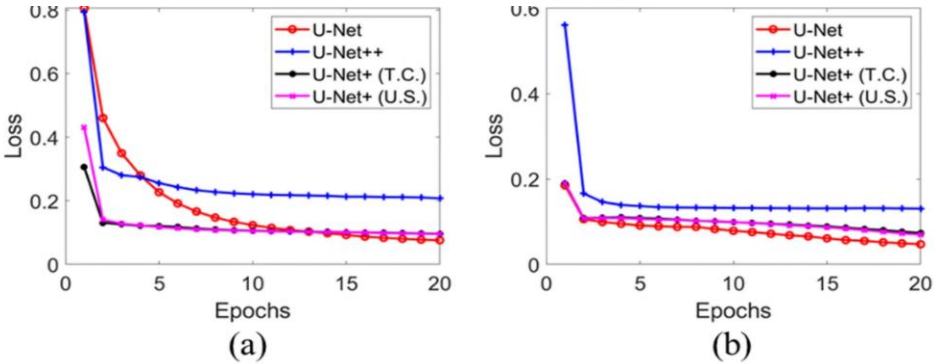

Fig. 3: Validation losses of different architectures, courtesy of (Long *et al*.,2020).

Huang *et al*., (2020) proposed an improved Unet3+ that provides for full-scale skip connections along with deeper supportive supervision. Low-level information from feature maps is combined with high-level understandings of these interconnections. The authors suggest that the network parameters for this U-Net be reduced to enhance computation efficiency. They also construct a classification-guided module and propose a hybrid loss function to improve the organ border and reduce over-segmentation.

Li *et al*., (2018) focused on the accurate and automated liver and tumour segmentation methods essential in clinical practice. While current 2D convolutions fail to fully utilize spatial information along in three dimensions (3D), and 3D convolutions are challenging due to high computational costs. To address these limitations, the authors propose a new hybrid high-density connection U-Net called Hdense U-Net. The model consists of a 2D high density U-Net for efficient feature extraction within lice and a 3D counterpart for aggregating the volume context of liver and tumour segmentation.

Size, shape, location variability, and poorly defined boundaries make segmentation of liver tumours challenging. 2D DenseU-Net integrates densely connected paths with U-Net connections, differentiating itself from DenseU-Net approaches by having U-Net connections added

between the encoder and decoder components. Consequently, the network enables the storage of low-level spatial features for better context exploration. The dataset used comprised 131 train images and 70 test images, all of which were 3D abdominal CT scans.

Weng *et al*., (2019) developed three types of basic operations based on search space to automatically locate two cell architectures for semantic image segmentation: DownSC and UpSC. It is inspired by the U-Net architecture. They show the results on three datasets: ultrasonic nerve datasets, magnetic resonance imaging datasets, and computed tomography datasets. Their architecture achieves greater performance with fewer parameters than U-Net without any pre-training.

Zeng *et al*., (2019) proposed a RIC-U-Net (residual inception channel attraction U-Net) for nucleus segmentation. To segment the nucleus better efficiently on RIC-U-net, residual blocks, multi-scale, and channel attention mechanisms are used. They also compare it to CP and Fiji, two standard CNN segmentation approaches. The Cancer Genomic Atlas dataset was used, which included thirty complete slide images. To generate regions dense in nuclei, the images are cropped into sub-images, each with a size of 1000x1000.

Developing more effective post-processing approaches to address the problem of cell overlap is of great importance. To achieve an accurate evaluation of the images in this study, we employ a two-step procedure: segmentation of the cell nuclei followed by segmentation of the entire cell. When the density of the cells in the microfluidic chamber is low, no overlap between different cells occurs. However, when the density exceeds a certain threshold, overlapping between the cytoplasm of different cells is notable. Despite this, the cell nuclei don't overlap, although contiguous nuclei are observed. Direct segmentation of the nuclei enables the accurate determination of correct cell number in each image. Other studies have utilized Faster-RCNN architectures for cell counting by focusing solely on the nucleus (Uka *et al*., 2020b). Cell imaging plays a crucial role in biomaterial risk assessment. A significant area of research focuses on quickly and personally assessing the biocompatibility of a biomaterial for patients receiving an implant. Although these measurements could be conducted using chemical tests, such methods may restrict other cell measurements. Therefore, microscopy is favoured as a non-invasive technique to replace invasive chemical tests on cells. In this work, we used images of cells in contact with polyarginine 50 (PAR50) and UniFast, two biomaterials commonly used in dentistry. We trained models for cell

segmentation and cell counting using U-Net architectures with various parameters. Based on the results, we selected the best optimizer and the best loss function was chosen for this specific dataset. The results of the cell shape parameters were then used to assess the relative toxicity of these biomaterials on cells.

2. MATERIALS AND METHODS

The health of Balb 3T3 cell in contact with different biomaterials is here analysed. Images are captured using a brightfield microscope, resulting in challenges such as low contrast, non-uniform background illumination etc. A total of 15 grayscale images, each with resolution of 1024x1280 pixels, were collected, representing a diverse range of cell shapes. Balb 3T3 cells exhibit a star- like morphology, characterized by a broad cytoplasm and clearly visible organelles within the nucleus.

Once the images were acquired, manual nucleus labelling and the entire cell (both the nucleus and the cytoplasm) subsequently occurred using APEER platform (https://www.apeer.com/app/). Representative images are in Figure 4 depicted. Nucleus identification is crucial, as it facilitates accurate counting of contiguous cells, even in cases of cytoplasm overlap.

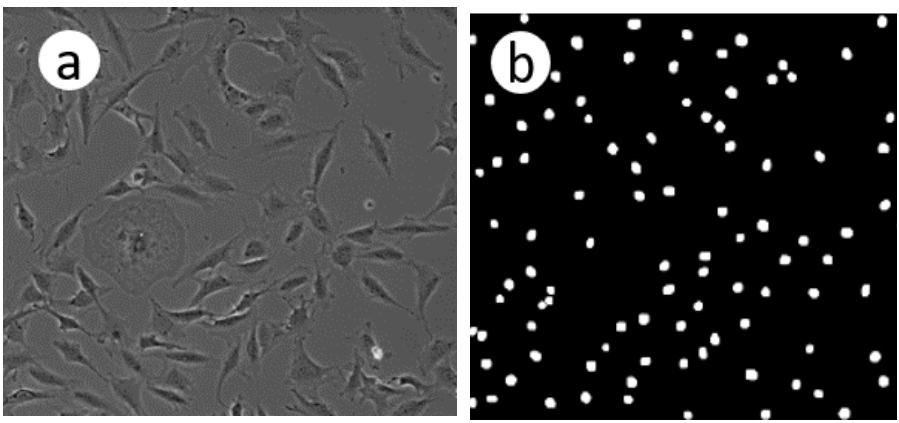

Fig. 4: Example of original images and the labelled images. Only the nuclei are labelled.

Figure 5 depicts the original images are cropped to size of 256x256 pixels, resulting in a total of 60 labelled images. Using cropped images

greatly reduces the computational complexity, as the runtime is proportional to the number of the pixels in an image times the number of the weights in the kernel.

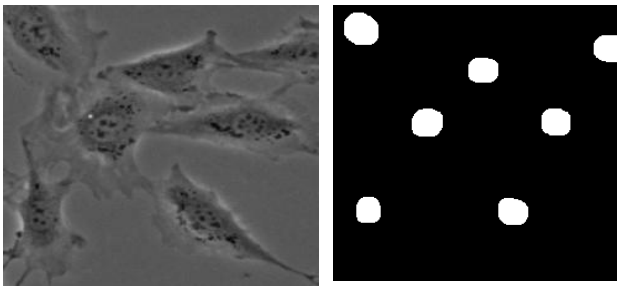

Fig. 5: Cropped images from the original and their masks.

The U-Net architecture is here employed to identify and segment the nuclei. This architecture utilizes encoders and decoders in a contracting and expanding path, respectively. Unlike architecture with dense layers, U-Net can process images of any size. During the expansive path, the images are resized to their original dimensions using the transposed convolution technique for up-sampling. The process is iteratively repeated until the image is transformed to satisfy the prediction requirements at the highest level of the architecture. The aim is to minimize the difference between the original and the reconstructed images. U-Net excels at image localization, performing by pixel-by-pixel predictions, and is particularly effective in generating good prediction even with a limited number of images (Ronnenberger *et al.*, 2015).

Table 1. U-NET model summary

Convolution layer 1	(256, 256, 1)
Max Pooling 1	(128, 128, 64)
Convolution layer 2	(128, 128, 128)
Max Pooling 2	(64, 64, 128)
Convolution layer 3	(64, 64, 256)
Max Pooling 3	(32, 32, 256)
Convolution layer 4	(32, 32, 512)
Max Pooling 4	(16, 16, 512)
Convolution layer 5	(16, 16, 1024)
Convolution layer 6	(32, 32, 512)

Convolution layer 7	(32, 32, 512)
Up sampling	(64, 64, 512)
Convolution layer 8	(64, 64, 256)
Convolution layer 9	(64, 64, 256)
Up sampling	(128, 128, 128)
Convolution layer 10	(256, 256, 1)

Semantic segmentation was first proposed in the 1970s as one of the most important research technologies for computer vision. It seeks to classify every pixel or point in the scene into many areas with specified semantic categories (Zhang *et al*., 2019).

The model in this work consists of 10 convolution layers and 4 max-pooling layers. Tables 1 present the architecture of the U-Net model, illustrating how the image size changes across the layers, as well as the corresponding parameters. The input size of the image is (256, 256, 1) and at the end of the bottleneck, it is reduced to (16,16,1024). The model is trained with for 100 epochs and the batch size is 4. Keras callbacks are used to implement: i) the weights are saved only if there is any improvement in the validation loss, and ii) the model will stop if there is no improvement in the validation loss. The training of the model was performed on NVIDIA GPU P4000, which is equipped with 1792 CUDA cores, 8 GB of GDDR5 memory and 243 GB/sec memory bandwidth. 31.031.685 parameters were used in this training.

3. RESULTS AND DISCUSSION

The models were trained using U-Net architecture in two phases. First, they were trained with labels/masks that included both the nucleus and the cytoplasm to determine the confluence (total area covered by the cells). Next, they were trained with labels/masks where only the nucleus was labelled. Then we have tested our dataset using these trained models were then tested in a dataset comprising 12 images, each with resolution of 1024x1280 pixels. The initial results of the testing phase identify the nuclei and also some artefacts are shown in the Figures 6-8.

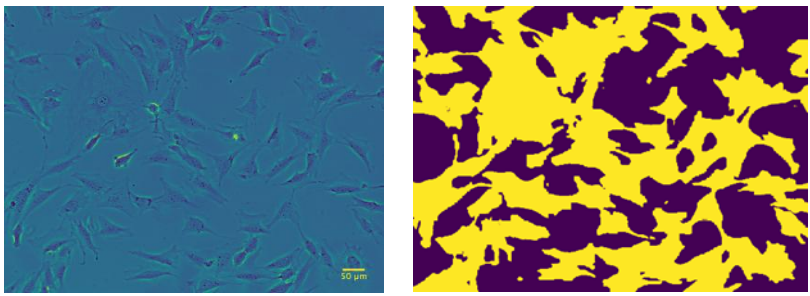

Fig. 6: Cell segmentation PAR50

Several optimizers were tested, but the Adam optimizer proved to be the most effective. This optimizer is widely used in deep learning tasks, and according to Jaber *et al*., (2022), it optimizes the entire hyperparameter space while keeping the optimizer function constant. In medical image datasets, when other functions outperformed the Adam optimizer, researchers have further optimized this function to achieve higher accuracy, demonstrating the potential of such a functions (Zhang *et al*., 2022). The effectiveness of the Adam optimizer is commonly reported not only in other studies focusing on microscopy medical images (Sun *et al*., 2024) but also in those involving photographic images (Rajput *et al*., 2023). Several loss functions were evaluated, with the binary cross-entropy loss function yielding the most optimal performance.

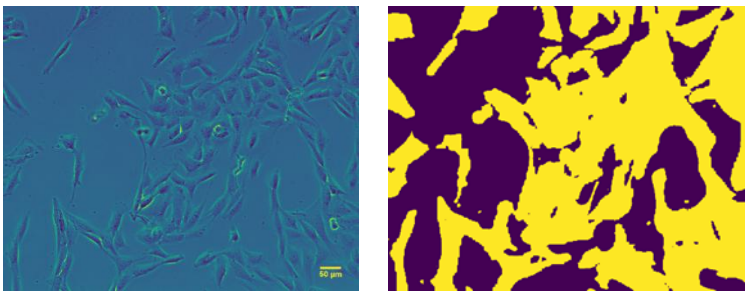

Fig. 7: Cell segmentation Unifast.

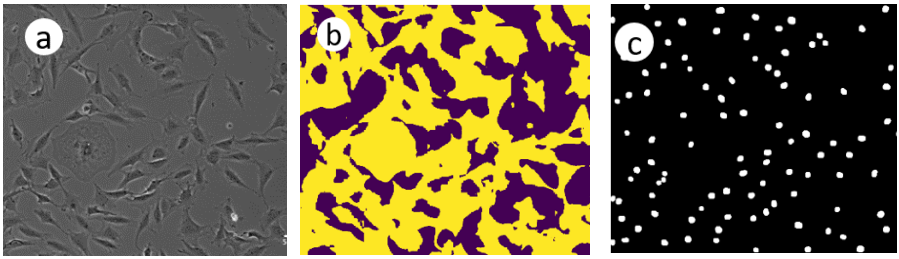

Fig. 8: PAR50 representative image (a) original image, (b) binary segmentation/area, (c) nuclei.

A post processing step is added to remove the artefacts. After identifying the objects from the model, the average object area is calculated. Any object with an area smaller than a threshold is removed. The dataset consists of 15 images in total, with three used for training and 12 left for evaluation purposes. Other studies have attempted to segment cells from brightfield images. For example, Ali *et al*., (2012) developed a series of algorithms to automatically segment HT1080 and HeLa cells, successfully identifying over 80% of the cells and over 75% of the nuclei. In our analysis of the dataset, we missed around 1-2% of the total cell count. In a similar attempt, Fishman *et al*., (2019) focused solely on segmenting the nuclei of A549 cell lines. In contrast, our work segments both the nucleus and the cytoplasm to determine the overall cell area, including both cell components: the nucleus and the deformable cytoplasm. The results are in Table 2 summarized. We have segmented the entire cell regions and counted the number of cells. By dividing the total confluency (in μm^2) by the number of cells, we calculated the average area per cell (see the fourth column in the Table 2). The cells in contact with PAR50 have an average area of 2940 μm^2, while cells in contact with UniFast have an average area of 1856 μm^2. If these areas were approximated circular, the corresponding radii would be 31 μm for PAR50 and 24 μm and UniFast. These results suggest that UniFast exhibits higher toxicity compared to the PAR50 biomaterial.

Table 2. Confluency, number of cells per image and average area per cell

Representative Images	Confluency (μm^2)	Number of cells	Area per cell
PAR50_01	229773,9	74	3105

PAR50_02	257468,8	87	2959
PAR50_03	292245,5	103	2837
PAR50_04	339722	110	3088
PAR50_05	228003,8	84	2714
Unifast_01	229218,1	125	1833
Unifast_02	156468,5	74	2114
Unifast_03	265640,8	164	1619

4. CONCLUSION

Cell imaging is a complex challenge, and its analysis and optimal quantitative evaluation depends on various factors including, experimental conditions, cell texture, cell conditions and also on the appropriate selection of the parameters for the training architecture. It is widely accepted in the literature that unstained brightfield images represent the most challenging set of images for deep learning techniques. Here, we performed cell counting and segmentation of cells in contact with two different biomaterials, PAR50 and UniFast to determine their relative toxicity. A series of combinations of different optimizers and loss functions were tested, and the best pair was selected for the images presented here. The combination of Adam optimizer and binary cross-entropy loss functions provided the highest accuracy. We evaluated the average area of the Balb/3T3 cells in the images, and from the area, we deduced that UniFast has a higher toxicity when compared to PAR50. Previous studies have reported the toxicity PAR50 is dose-dependent, with high doses of polyarginine causing membrane disruption and cell death (Mitchel *et al*., 2000). Other previous studies have indicated that UniFast toxicity is associated with residual monomer leaching (Leggat *et al*., 2003).

ACKNOWLEDGEMENT

This project received funding from the European Union's Horizon 2020 Research and Innovation Program under Grant Agreement No. 760921 (PANBioRA).

REFERENCES

Ali R, Gooding M, Szilágyi T, Vojnovic B, Christlieb M, Brady M. 2012. Automatic segmentation of adherent biological cell boundaries and nuclei from brightfield microscopy images. *Machine Vision and Applications*, **23:** 607–621 (2012). https://doi.org/10.1007/s00138-011-0337-9.

Baysoy A, Zhiliang B, Rahul S, Rong F. 2023.The technological landscape and applications of single-cell multi-omics. *Nature Reviews Molecular Cell Biology*, **24 (10):** 695-713.

Budginaitė E, Mindaugas M, Arvydas L, Povilas T. 2021. Deep learning model for cell nuclei segmentation and lymphocyte identification in whole slide histology images. *Informatica*, **32 (1):** 23-40. DOI:10.15388/20-INFOR442Corpus ID: 231813406.

Caicedo JC, Goodman A, Karhohs KW, Cimini BA, Ackerman J, Haghighi, M, Carpenter AE. 2019. Nucleus segmentation across imaging experiments: the 2018 Data Science Bowl. *Nature methods*, **16(12):** 1247-1253.

Chmayssem A, Mourier V, Verplanck N, Uka A, Polisi Xh, Halili A, Muller C, Petit L, Mailley P. 2021. Integrated on chip cytotoxicity test with real-time image analysis and electrochemical sensors-based monitoring. Organ-On-Chip (EUROoCS 2021), 1, 1.

Chmayssem A, Tanase CE, Verplanck N, Gougis M, Mourier V, Zebda A, Mailley P. 2022. New microfluidic system for electrochemical impedance spectroscopy assessment of cell culture performance: design and development of new electrode material. *Biosensors*, **12(7):** 452.

Dincer C, Chandra P, Morales-Narváez E. 2022. Integrated biosensors towards clinical and point-of-care diagnostics. Frontiers in Bioengineering and Biotechnology, 10, 1008603.

Dollinger C, Ndreu-Halili A, Uka A, Singh S, Sada H, Neuman T, Vrana NE. 2017. Controlling incoming macrophages to implants: responsiveness of macrophages to gelatin micropatterns under M1/M2 phenotype defining biochemical stimulations. *Advanced Biosystems*, **1(6):** 1700041.

Fishman D, Salumaa SO, Majoral D, Peel S, Wildenhain J, Schreiner A, Parts L. 2019. Segmenting nuclei in brightfield images with neural networks. bioRxiv, 764894.

Gribova V, Dominguez JMA, Morin A, Diaz JS, Lavalle P, Vrana NE. 2023. A miniaturized genotoxicity evaluation system for fast

biomaterial-related risk assessment. *Analytical Methods*, **15(12):** 1584-1593.

Göröcs Z, Tamamitsu M, Bianco V, Wol P, Roy S, Shindo K, Ozcan, A. 2018. A deep learning-enabled portable imaging flow cytometer for cost-effective, high-throughput, and label-free analysis of natural water samples. *Light: Science and Applications*, **7(1):** 66.

Huang H, Lin L, Tong R, Hu H, Zhang Q, Iwamoto Y, Wu J. 2020. Unet 3+: A full-scale connected unet for medical image segmentation. In ICASSP 2020-2020 IEEE international conference on acoustics, speech and signal processing (ICASSP) (pp. 1055-1059). IEEE.

Zhang J, Xiaoli Zh, Zheng Ch, Zhejun L. 2019. A review of deep learning-based semantic segmentation for point cloud. IEEE access 7 (2019): 179118-179133.

Krizhevsky A, Sutskever I, Hinton GE. 2017. ImageNet classification with deep convolutional neural networks. *Communications of the ACM*, **60(6):** 84-90.

Leggat PA, Kedjarune U. 2003. Toxicity of methyl methacrylate in dentistry. *International dental journal*, **53(3)**: 126-131.

Li L, Li Y, Shao Z, Luo G, Ding M, Liang, Q. 2018. Simultaneous assay of oxygen-dependent cytotoxicity and genotoxicity of anticancer drugs on an integrated microchip. *Analytical chemistry*, **90(20):** 11899-11907.

Li X, Chen H, Qi X, Dou Q, Fu CW, Heng PA. 2018. H-DenseUNet: hybrid densely connected UNet for liver and tumor segmentation from CT volumes. *IEEE transactions on medical imaging*, **37(12):** 2663-2674.

Long, F. (2020). Microscopy cell nuclei segmentation with enhanced U-Net. BMC *Bioinformatics* **21(1):** 8.

Magnusson EB, Halldorsson S, Fleming RM, Leosson K. 2013. Real-time optical pH measurement in a standard microfluidic cell culture system. *Biomedical optics express*, **4(9):** 1749-1758.

Martin C, Altman LE, Rawat S, Wang A, Grier DG, Manoharan VN. 2022. In-line holographic microscopy with model-based analysis. *Nature Reviews Methods Primers*, **2(1):** 83.

Mitchell DJ, Steinman L, Kim DT, Fathman CG, Rothbard JB. 2000. Polyarginine enters cells more efficiently than other polycationic homopolymers. *The Journal of Peptide Research*, **56(5):** 318-325.

Ozcan A. 2014. Mobile phones democratize and cultivate next-generation imaging, diagnostics and measurement tools. Lab on a Chip, **14(17)**: 3187-3194.

Polisi X, Avdiu D, Uka A, Halili N, Kollcaku K, Ciulla C. 2023. Evaluation of Cell Segmentation Using Pruning and Quantization. In 2023 International Conference on Computing, Electronics & Communications Engineering (iCCECE) (pp. 139-144). IEEE.

Polisi X, Halili AN, Uka A, Ciulla C. 2023. Two-Stage Unsupervised Classification of Cell Health. In 2023 International Conference on Computing, Electronics & Communications Engineering (iCCECE) (pp. 145-149). IEEE.

Polisi X, Halili A, Tanase CE, Uka A, Vrana NE, Ghaemmaghami A. 2020. Computer Assisted Analysis of the Hepatic Spheroid Formation. In Computational Bioengineering and Bioinformatics: Computer Modelling in Bioengineering 8 (pp. 117-126). Springer International Publishing.

Rajput PK, Ravulakollu KK, Jagadam N, Singh P. 2023. Adam optimizer based deep learning approach for improving efficiency in license plate recognition. In Automation and Computation (pp. 439-449). CRC Press.

Rodrigues NP, Sakai Y, Fujii T. 2008. Cell-based microfluidic biochip for the electrochemical real-time monitoring of glucose and oxygen. *Sensors and Actuators B: Chemical*, **132(2):** 608-613.

Ronneberger O, Fischer P, Brox T. 2015. U-net: Convolutional networks for biomedical image segmentation. In Medical image computing and computer-assisted intervention–MICCAI 2015: 18th international conference, Munich, Germany, October 5-9, 2015, proceedings, part III 18 (pp. 234-241). Springer International Publishing.

Schurr J, Haghofer A, Lanzerstorfer P, Winkler S. 2022. Automated Segmentation of Patterned Cells in Micropatterning Microscopy Images. In International Joint Conference on Biomedical Engineering Systems and Technologies (pp. 34-52). Cham: Springer Nature Switzerland.

Siddique N, Paheding S, Elkin CP, Devabhaktuni V. 2021. U-net and its variants for medical image segmentation: A review of theory and applications. *IEEE access*, **9:** 82031-82057.

Sun H, Zhou W, Yang J, Shao Y, Xing L, Zhao Q, Zhang L. 2024. An Improved Medical Image Classification Algorithm Based on Adam Optimizer. *Mathematics*, **12(16):** 2509.

Tovar M, Mahler L, Buchheim S, Roth M, Rosenbaum MA. 2020. Monitoring and external control of pH in microfluidic droplets during microbial culturing. *Microbial cell factories*, **19**: 1-9.

Uka A, Imeraj G, Qesaraku B, Shehu B. 2022. Fourier Ptychography Microscopy Resolution Improvement Employing Refocusing. In BIODEVICES (pp. 191-195).

Uka A, Ndreu Halili A, Polisi X, Topal AO, Imeraj G, Vrana NE. 2021. Basis of image analysis for evaluating cell biomaterial interaction using brightfield microscopy. *Cells Tissues Organs*, **210(2):** 77-104.

Uka A, Polisi X, Barthes J, Halili AN, Skuka F, Vrana NE. 2020. Effect of Preprocessing on Performance of Neural Networks for Microscopy Image Classification. In 2020 International Conference on Computing, Electronics & Communications Engineering (iCCECE) (pp. 162-165). IEEE.

Uka A, Polisi X, Halili A, Dollinger C, Vrana NE. 2017. Analysis of cell behavior on micropatterned surfaces by image processing algorithms. In IEEE EUROCON 2017-17th International Conference on Smart Technologies (pp. 75-78). IEEE.

Uka A, Tare A, Polisi X, Panci I. 2020. FASTER R-CNN for cell counting in low contrast microscopic images. In 2020 International Conference on Computing, Networking, Telecommunications & Engineering Sciences Applications (CoNTESA) (pp. 64-69). IEEE.

Uka A, Topalli G, Hoxha J, Vrana NE. 2021. FPGA Implementation of Filters in Medical Imaging. In BIODEVICES (pp. 195-200).

Weng Y, Zhou T, Li Y, Qiu X. 2019. Nas-unet: Neural architecture search for medical image segmentation. *IEEE access*, **7**: 44247-44257.

Whitesides GM. 2006. The origins and the future of microfluidics. *Nature*, **442(7101):** 368-373.

Zeng Z, Xie W, Zhang Y, Lu Y. 2019. RIC-Unet: An improved neural network based on Unet for nuclei segmentation in histology images. *IEEE Access*, **7**: 21420-21428.

Zhang Z. 2018. Improved adam optimizer for deep neural networks. In 2018 IEEE/ACM 26th international symposium on quality of service (IWQoS) (pp. 1-2). *IEEE*.

Rane AS, Rutkauskaite J, deMello, A, Stavrakis S. 2017. High-throughput multi-parametric imaging flow cytometry. *Chem*, **3(4):** 588-602. https://doi.org/10.1016/j.chempr.2017.08.005 .